



# Plasmonic Ag nanoparticles and p-type CuO-modified ZnO nanorods for efficient photoelectrochemical water splitting

Chonghao Ma<sup>1,2</sup> · Zhifeng Liu<sup>1,2</sup> · Zhengfu Tong<sup>1,2</sup> · Changcun Han<sup>1,2</sup> · Qijun Cai<sup>1,2</sup>

Received: 7 March 2019 / Accepted: 29 May 2019 / Published online: 4 June 2019  
© Springer-Verlag GmbH Germany, part of Springer Nature 2019

## Abstract

The light absorption range of semiconductor materials and the separation rate of electron–hole pairs are significant challenges in photoelectrochemical (PEC) water splitting. In this work, we first prepared a ternary heterojunction of ZnO/CuO/Ag by chemical bath deposition method. The formation of the heterojunction can improve the absorption range and increase the electron–hole pairs' separation rate, and the loading of plasmonic Ag nanoparticles can expand the absorption range of visible light and generate more photogenerated electrons through surface plasmon resonance (SPR). The ZnO/CuO/Ag heterojunction photoelectrode reveals an efficient photocurrent density of  $3.45 \text{ mA cm}^{-2}$  at 1.23 V vs. RHE, which is 3.08 and 1.12 times higher compared with ZnO and ZnO/CuO photoelectrode, respectively. This study shows that the simultaneous reaction of heterojunction and plasmonic noble metal nanoparticles can synergistically improve the photoelectric properties of photoanodes in photoelectrochemical water-splitting system.

## 1 Introduction

Photoelectrochemical (PEC) water splitting is a technology that converts solar energy into chemical energy, which decomposes water into hydrogen ( $\text{H}_2$ ) and oxygen ( $\text{O}_2$ ) [1–5]. The first breakthrough progress on hydrogen production was demonstrated by Fujishima and Honda using n-type  $\text{TiO}_2$  photoelectrode in 1972 [6]. Subsequently, the selection of a variety of semiconductor materials, for instance, ZnO [7],  $\text{Fe}_2\text{O}_3$  [8],  $\text{BiVO}_4$  [9] etc., has been intensively and diversely chosen for synthesis into photoelectrodes for PEC water splitting. Among all of these semiconductor materials, ZnO has become one of the most potential optical electrode [10–12] due to the low cost, superior chemical stability, non-toxicity, and high photoelectrocatalysis activity. For example, Law M et al. prepared crystalline ZnO nanowires and proved that they have high photoelectric performances [13].

However, ZnO is a wide bandgap ( $E_g = 3.2 \text{ eV}$ ) semiconductor, and its low quantum efficiency and limited optical

absorption range severely limit its effective PEC water decomposition [14]. Fortunately, the formation of a heterojunction with a narrow bandgap semiconductor can broaden the photoresponse range and increase the separation rate of electron–hole pairs [15]. Based on these theories, there are some narrow bandgap semiconductor such as  $\text{Sb}_2\text{S}_3$  [16], CdS [17],  $\text{Cu}_2\text{O}$  [18] etc., which are used to improve the PEC performances of ZnO. CuO is a semiconductor can with a bandgap of 1.8 eV, which can better broaden the visible light absorption range. There are some records, showing that the use of CuO can significantly improve the optoelectronic properties of ZnO. Ng et al. prepared the tungsten trioxide ( $\text{WO}_3$ ) and copper(II) oxide (CuO) photoelectrodes from acidic aqueous solution of peroxy-tungstate and basic aqueous solution of copper sulfate–lactic acid, respectively, by electrodeposition method, and its photocurrent reached  $0.16 \text{ mA cm}^{-2}$  at 0.7 V vs. RHE [19]. Wang et al. reported that the growth of ZnO branched nanowires on the CuO nanowires and the fabrication of p-CuO/n-ZnO heterojunction nanostructured photodetector (PD), and it was found that turning on voltage of the fabricated PD reduced from  $\sim 0.7$  to  $\sim 0.2$  V under ultraviolet (UV) illumination [20].

In addition, noble metals and compound play an important role in improving the photoelectric properties of semiconductor materials, such as noble metal oxides or sulfides ( $\text{RuO}_2$  [21],  $\text{IrO}_2$  [22], and PdS [23]). They can play an

✉ Zhifeng Liu  
tjulzf@163.com

<sup>1</sup> Hubei Collaborative Innovation Center for High-Efficiency Utilization of Solar Energy, Hubei University of Technology, Wuhan 430068, China

<sup>2</sup> School of Science, Hubei University of Technology, Wuhan 430068, China

important role in improving the photoelectrocatalytic performances of water decomposition, which act as cocatalyst [24]. Of particular interest is the use of noble metal nanoparticles (NPs) to increase the rate of separation of photogenerated electron–hole pairs, thereby enhancing photocatalytic activity. This is due to better charge separation, that is, electrons generated by light tend to accumulate on the metal member, while the holes remain on the surface of the photoelectrode [25–27]. In addition, in plasmon-induced optoelectronic analysis, noble metal nanoparticles (such as Ag and Au) can absorb visible light by surface plasmon resonance (SPR). Chen et al. mainly focused on the perspective of molding devices through exploring new materials and novel architectures inspired by the state-of-the-art UV photodetectors, predicting the direction of the next-generation photodetectors [28]. Ahmadvand et al. reported that calculating the plasmonic and photothermal responses of metallic cluster, it is possible to achieve thermal heat flux generation of  $64.7 \mu\text{W cm}^{-2}$  and temperature changes in the range of  $\Delta T = 150 \text{ K}$ , using Fano resonant effect [29]. Tanzid et al. combined hot-carrier-based photodetection with free-carrier absorption (FCA) in highly doped p-type Si to create a narrowband, near-infrared, photodetector architecture with enhanced performance [30]. Zheng et al. reported the successful synthesis of highly ordered porous  $\alpha\text{-Fe}_2\text{O}_3/\text{Au}$  nanotube arrays by a simple method. Benefitting from the plasmonic effect, and unique aligned porous structural features, the  $\alpha\text{-Fe}_2\text{O}_3/\text{Au}$  NTAs have high efficiency and stable operation performance, thus leading to significant catalytic activity for photoelectrochemical methanol oxidation, and the Faraday efficiency is 79.23% that shows better photoelectrochemical performance [31]. At present, silver (Ag) nanoparticles have attracted much attention due to their special SPR characteristics and remarkable photostability, which can interact with light in the visible and near-infrared regions [32]. In a related study, Chaudhary et al. prepared a ternary Ag/TiO<sub>2</sub>/CNT photoanode grafting Ag nanoparticles (NPs) on the surface of as-synthesized TiO<sub>2</sub>/CNT nanocomposite for the photoelectrochemical (PEC) water splitting under visible light irradiance, and its photocurrent reached  $0.91 \text{ mA}\cdot\text{cm}^{-2}$  at 1.23 V vs. RHE (1.23 V is the potential of the standard hydrogen electrode to water splitting) [33].

In this work, ternary ZnO/CuO/Ag heterojunction photoelectrodes were first successfully synthesized through chemical bath deposition method. The as-prepared ZnO/CuO/Ag heterojunctions possess high photoelectric performance under visible light. In comparison with the previously reported ZnO photoelectrode, the ZnO/CuO/Ag heterojunction is superior in two aspects for efficient photoelectrochemical water-splitting reactions: (i) the formation of a heterojunction can effectively expand visible light absorption range, and Ag NPs can also promote this process due to the surface plasmon resonance (SPR) and (ii) the formation of

a heterojunction can form a gradient energy level, which can better promote the separation of electron–hole pairs. Under visible light irradiation, Ag NPs generate hot electrons due to the SPR effect, and the hot electrons are injected to the conduction bands of ZnO/CuO heterojunction that can make electron–hole pairs better separate.

## 2 Experimental section

### 2.1 Preparation of ZnO nanorod arrays' (NRs') films

ZnO NRs were directly grown on indium tin oxide glass substrates (ITO glass). The ITO was ultrasonically washed for 15 min with deionized water, acetone, and isopropyl alcohol. First, the ZnO seed layer was obtained by the pulling method. Then, the as-prepared seed layer was calcined in a muffle furnace for 1 h. A mixture solution for growing ZnO NRs was prepared by dissolving 0.005 M zinc nitrate hexahydrate, 0.005 M hexamethylenetetramine. Subsequently, the seed layer was placed in a container and the NRs were grown by chemical bath deposition at 90 °C for 4 h. Finally, the ZnO NRs' samples were rinsed with deionized water [34].

### 2.2 Preparation of ZnO/CuO heterojunction

The synthesized ZnO/CuO heterojunction was fabricated by chemical bath deposition method. First, 5 mM copper(II) nitrate hydrate and 5 mM hexamethylenetetramine (HMTA) were mixed and transferred into a vial. Second, the substrates coated with ZnO nanorod arrays were transferred into the prepared vial. The vial was then heated at 95 °C for 1, 2, and 3 h, respectively. Finally, the final product was dried in an oven at 100 °C.

### 2.3 Preparation of ZnO/CuO/Ag heterojunction

First, the ZnO/CuO heterojunction heated for 3 h acted as substrate. Then, 4 mM silver nitrate (AgNO<sub>3</sub>) and 4 mM sodium citrate (Na<sub>3</sub>C<sub>6</sub>H<sub>5</sub>O<sub>7</sub>·2H<sub>2</sub>O) were mixed and transferred into a vial. The prepared solution was transferred to a vial and the substrate (ZnO/CuO heterojunction) was placed obliquely at the bottom of the vial. The vial was then heated at 100 °C for 1 h. Finally, the prepared sample was dried in an oven.

### 2.4 Characterization

The structures of the samples were characterized by scanning electron microscopy (SEM), and the morphologies of the samples were characterized by transmission electron microscopy (TEM). The crystal structures and chemical

element compositions were explored by X-ray diffractometry (XRD) and energy-dispersive spectroscopy (EDS). The ultraviolet–visible (UV–vis) spectrum was measured to measure the absorbance of the samples.

The PEC data of the samples were measured using a three-electrode electrochemical workstation with a platinum foil as the counter electrode and Ag/AgCl electrode reference electrode. The samples were linearly scanned in 0.4 M sodium sulfate ( $\text{Na}_2\text{SO}_4$ ) electrolyte, under simulated sunlight illumination at  $100 \text{ mW/cm}^2$  from a 300 W xenon lamp.

The measured potential vs. the Ag/AgCl reference electrode was converted to the reversible hydrogen electrode (RHE) scale after electrochemical measurements using the Nernst equation:

$$E_{\text{RHE}} = E_{\text{Ag/AgCl}} + 0.0591 \times \text{pH} + E'_{\text{Ag/AgCl}}(3.0\text{M KCl}), \quad (1)$$

where  $E'_{\text{Ag/AgCl}}(3.0 \text{ M KCl}) = 0.210 \text{ V}$  at  $25 \text{ }^\circ\text{C}$  [35].

### 3 Results and discussion

Figure 1 shows scanning electron microscopy images of initial ZnO and ZnO/CuO samples immersed at  $95 \text{ }^\circ\text{C}$  for different times. As shown in Fig. 1a, the initial ZnO is in the shape of a regular hexahedral nanorod with the diameter of about 100 nm. Figure 1b–d shows a top view of ZnO/CuO samples bathed at  $95 \text{ }^\circ\text{C}$  for 1, 2, and 3 h, respectively.

It can be seen that the diameter of ZnO nanorods is about 100 nm, and CuO is dendritic distributing on the surface of ZnO nanorods with diameter of about 20, 30, and 35 nm. The increase in the size of CuO can be attributed to the increase of temperature of the growth solution. This result indicates that the reaction product increases, as the bath time increases, resulting in an increase in CuO size. The above data show that the heterostructure of ZnO/CuO can be obtained by precise control of the bath time.

The microstructure information of ZnO/CuO was revealed by TEM and HRTEM further, as shown in Fig. 2. As shown in Fig. 2a, CuO particles are connected with ZnO and distributed in a dendritic shape. The HRTEM image shown in Fig. 2b and the lattice fringes of each material are easily observed. The measured lattice spacing is 0.247 nm and 0.253 nm, respectively, which can be correlated with the (111) plane of ZnO and the (101) plane of CuO.

Figure 3 shows the XRD patterns of the as-prepared samples. It can be clearly seen that there is one characteristic peaks at  $2\theta$  values of  $36.4$ , corresponding to the (101) crystal face of CuO (JCPDS 44-0706), and the X-ray diffraction peak of the ZnO film prepared on the ITO group was correlated with the characteristic peak of the diamond-shaped ZnO (JCPDS 77-0191).

To determine the specific content of the elements, an energy spectrum (EDS) test was performed. As shown in Fig. 4a–c, the Cu-element ratio in the ZnO/CuO heterostructure is about 7.72, 10.93, and 13.07%, respectively. The change in Cu content can be attributed to time control,

**Fig. 1** SEM images of the samples. **a** ZnO and **b–d** for ZnO/CuO samples bathed at  $95 \text{ }^\circ\text{C}$  for 1 h, 2 h, and 3 h, respectively

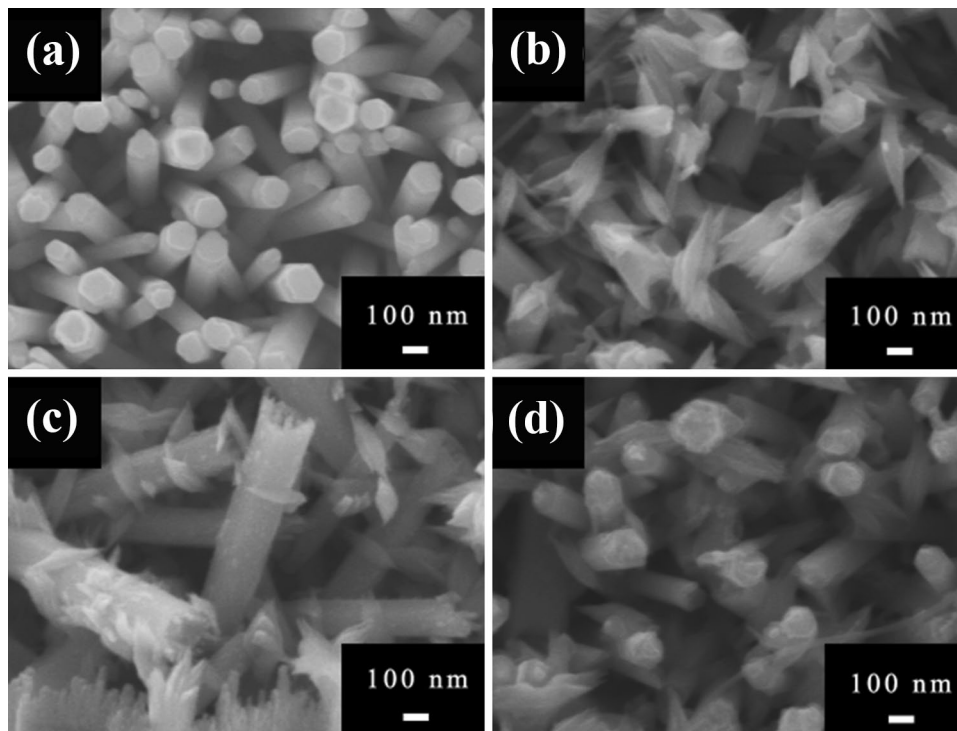


**Fig. 2** TEM **a** and HRTEM image **b** of ZnO/CuO

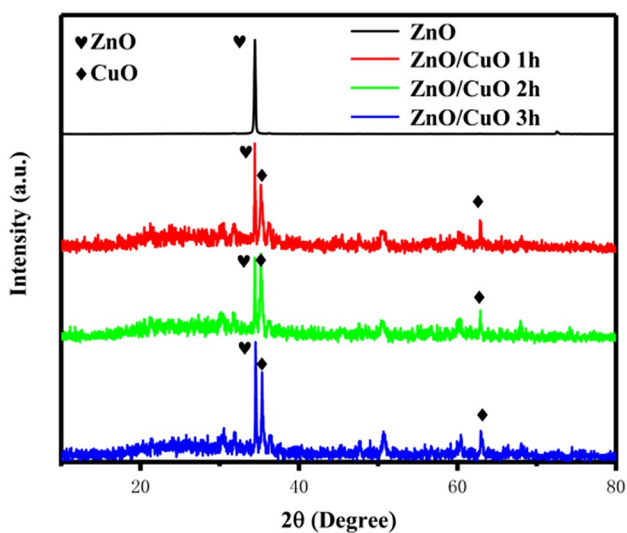
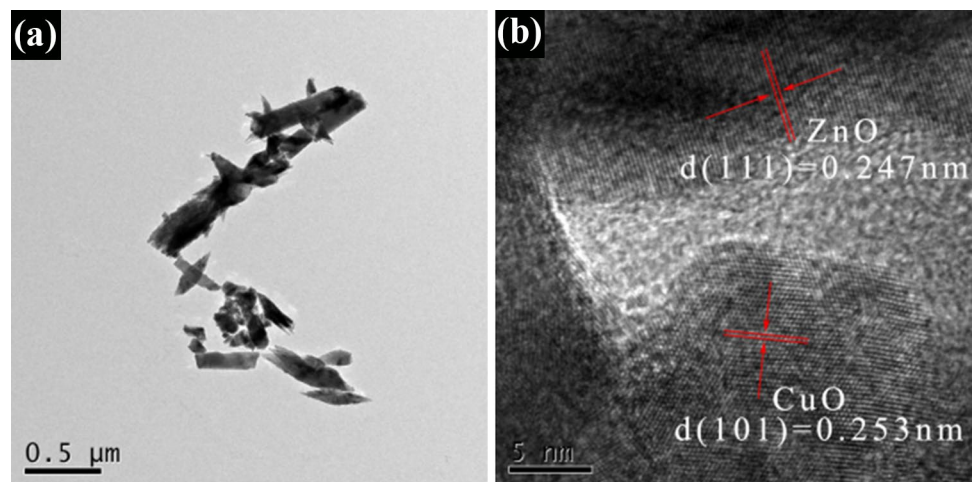


**Fig. 3** X-ray diffraction patterns of the ZnO nanorod and ZnO/CuO heterojunction bathed for 1 h, 2 h, and 3 h, respectively

indicating that the longer the bath time is, the higher the Cu content is.

Figure 5a shows the absorbance spectra of the as-prepared ZnO and ZnO/CuO heterostructures bathed at 95 °C for different times. The absorption edge of ZnO is estimated to be 385 nm (Fig. 4a). After forming a ZnO/CuO heterojunction, the absorption edge shift from about 385 nm to 467, 476, and 496 nm, corresponding to ZnO/CuO bathed for 1, 2, and 3 h, respectively. The prepared ZnO/CuO heterostructures exhibit intense absorption in the visible light region. The bandgap energy of the samples was estimated from the intercept of the extrapolated linear part of  $(ah\nu)^2$  vs. photon energy (see Fig. 5b). The estimated bandgap energy is approximately 3.4 eV for ZnO, 2.6 eV for ZnO/CuO (1 h), 2.55 eV for ZnO/CuO (2 h), and 2.4 eV for ZnO/CuO (3 h). This is because that the formation of a heterojunction in

combination with the narrow bandgap semiconductor CuO increases the visible light absorption range and thus absorbing more visible light.

The PEC data of the samples were measured in a three-electrode electrochemical workstation, using a platinum foil as the counter electrode and Ag/AgCl electrode reference electrode. Figure 5c shows current density–voltage ( $i$ - $v$ ) curves for ZnO and ZnO/CuO at different bath times for simulated and non-simulated light conditions. The dark-current density–voltage ( $i$ - $v$ ) curves of both ZnO and ZnO/CuO show negligible currents, so we can determine that the illumination of the light affects the photoelectron movement. As shown in Fig. 5c, the photocurrent density–voltage curves of ZnO and ZnO/CuO show that the photocurrent density of the ZnO/CuO heterostructure is higher than that of the ZnO electrode ( $1.12 \text{ mA cm}^{-2}$ ) at 1.23 V vs. RHE. As the size of the dendritic CuO increases, the reaction surface area increases, which in turn causes dark current and photocurrent increase with the immersion time. Figure 5d shows the transient current density of the corresponding heterostructure with chopping at 1.23 V vs. RHE, which shows a good switching behavior. The photocurrents of all four photoelectrodes exhibit a rapid rise and fall trend at the beginning and end of each chopping wave, indicating that the carrier transport rate in the photoanode is very fast. The above results show that the formation of heterojunction between CuO and ZnO can effectively improve the photoelectric properties of ZnO NRs.

As shown in Fig. 6, it is a top view and a cross-sectional SEM image of ZnO/CuO/Ag, respectively. It is clear that the Ag is uniformly distributed on the ZnO nanorods and CuO branches, showing a circular shape with a size of about 20 nm. From the cross-sectional SEM images, we can also see that little Ag particles are attached to the ZnO/CuO heterostructures. The prepared Ag NPs' (~20 nm) colloid exhibits a relatively bright white color. EDS testing can be used to dedicate the specific content of various elements.

**Fig. 4** a–c for EDS spectrum of the ZnO/CuO film for 1 h, 2 h, and 3 h. The inset is the atom percent of O, Cu, and Zn

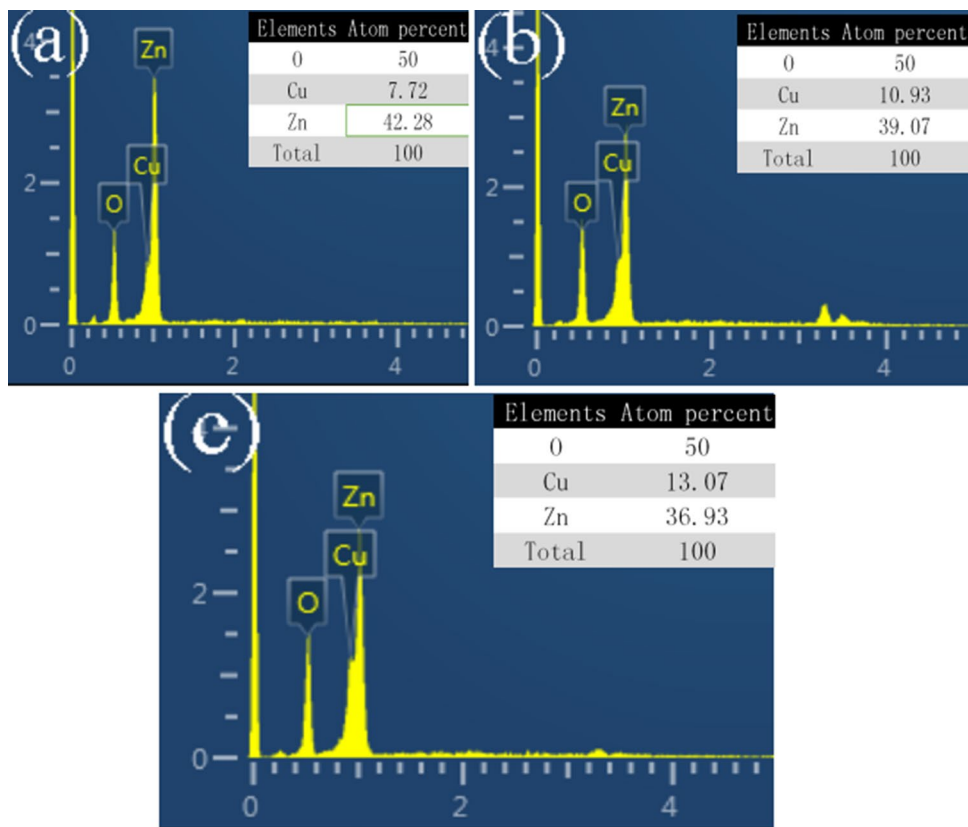


**Fig. 5** UV–visible light absorption spectra of ZnO/CuO (a) and curves of  $(\alpha h\nu)^2$  vs.  $h\nu$  (b); (c) current density–voltage (*i*–*v*) curves under simulated sunlight illumination and in dark; and (d) photocurrent density – time curves (*i*–*t*) curves measured at 1.23 V vs. RHE under chopped simulated sunlight illumination

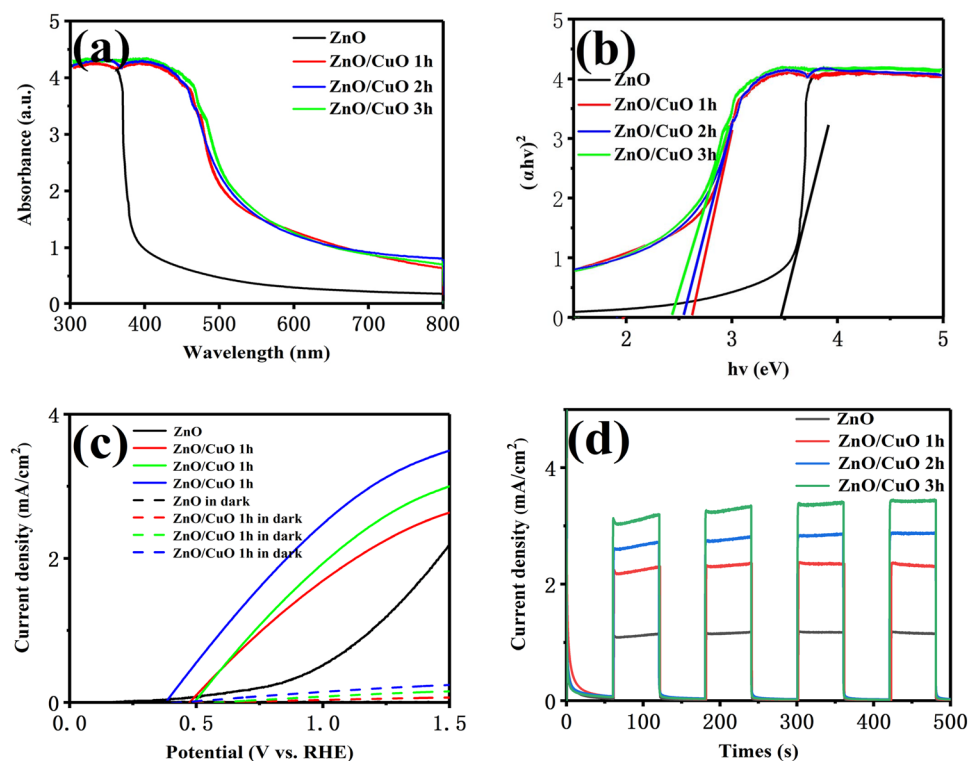


**Fig. 6** SEM images of **a** ZnO/CuO/Ag and **b** cross-sectional SEM image of ZnO/CuO/Ag

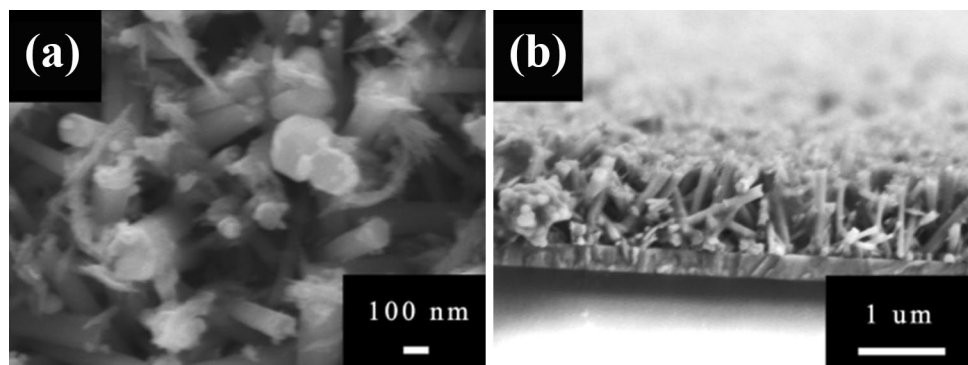
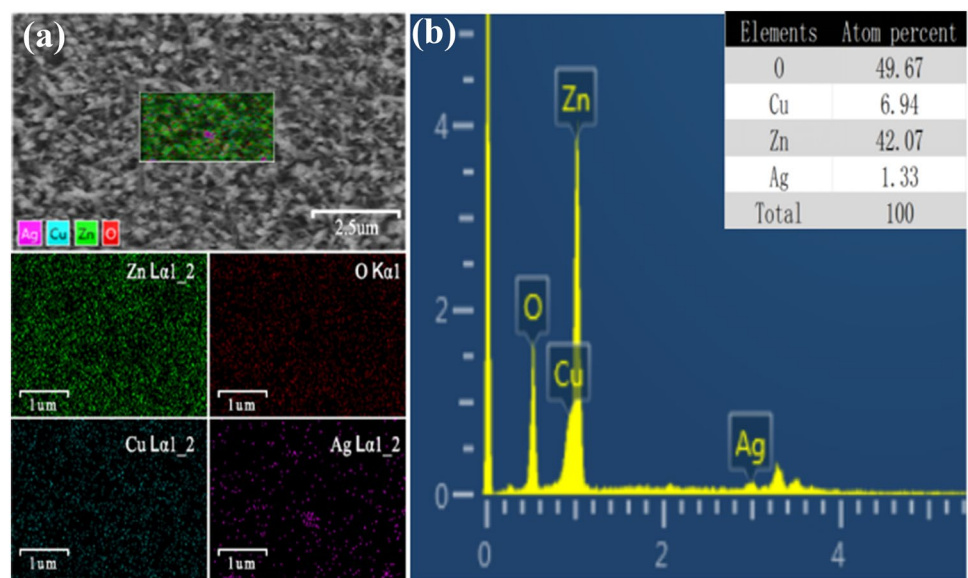


Figure 7a shows the EDS spectrum of the ZnO/Cu/Ag heterostructure. In addition, Fig. 7b shows the elemental mapping of the constituent atoms, which are evenly distributed throughout the heterostructure and confirms the presence of Zn, O, Cu, and Ag in the heterostructure. The elemental percentages of Zn, O, Cu, and Ag are 49.67, 6.94, 42.07, and 1.33, respectively. This result further proves that a small amount of Ag adhere to the ZnO/CuO heterojunction, corresponding to the SEM image of Fig. 6.

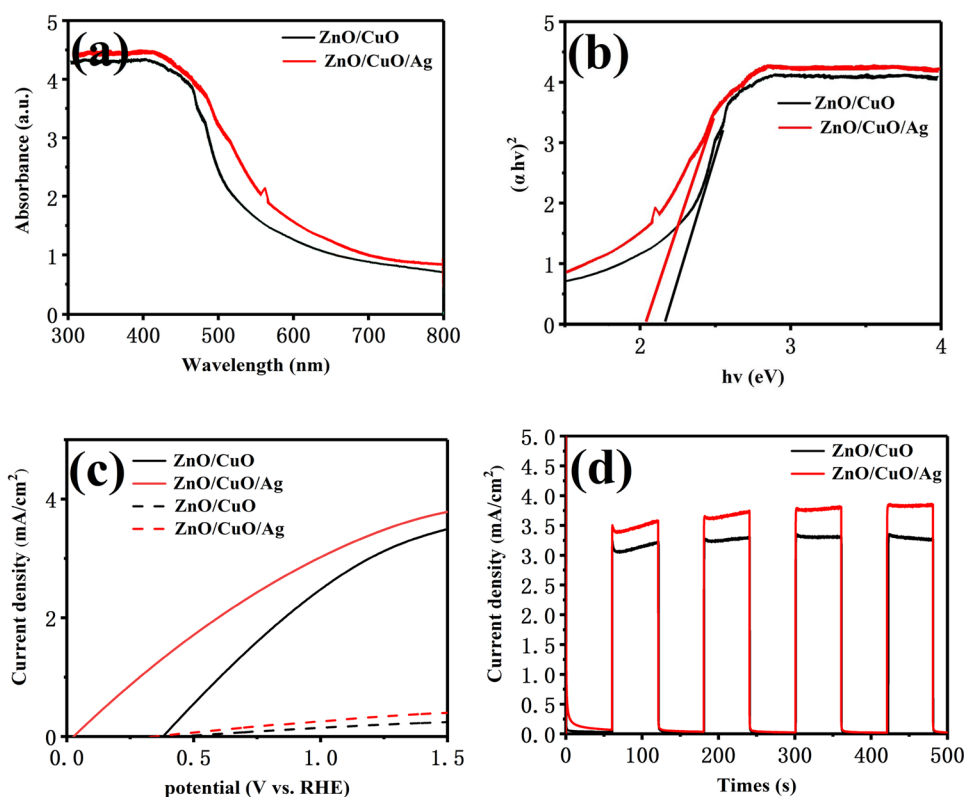
As shown in Fig. 8b, the bandgap energy of ZnO/CuO/Ag is about 2.05 eV. Figure 8a shows the absorbance spectra of a ZnO/CuO/Ag heterojunction. Loading the plasmonic Ag NPs (~20 nm) onto ZnO/CuO slightly increases its absorption in the visible light band due to the SPR effect of Ag NPs. In addition, the ZnO/CuO/Ag curve has a small peak at a wavelength of 500 nm. According to the relevant Ref. [36], the plasma absorption peak is caused by collective oscillation of free conduction band electrons induced by incident electromagnetic radiation in Ag NPs, the UV–visible spectrum of sample also indirectly proves that Ag NPs have been deposited on ZnO/

CuO. Meanwhile, as shown in Fig. 8b, the bandgap of the ZnO/CuO/Ag heterojunction is narrower than ZnO/CuO, and the bandgap is about 2.1 eV. This result indicates that combining the plasmonic Ag NPs with the ZnO/CuO heterostructure can significantly broaden the visible light absorption range of the heterojunction. To further demonstrate the effect of Ag NPs on the separation efficiency of photogenerated electrons and holes, we performed photocurrent tests. As shown in Fig. 8c, the photocurrent density follows the order of ZnO/CuO/Ag > ZnO/CuO, and about  $3.45 \text{ mA cm}^{-2}$  of ZnO/CuO/Ag. According to some literatures, the separation efficiency of the photogenerated electron–hole pairs will increase when the optical response signal becomes high [37]. PEC measurements show that the loading of Ag nanoparticles has a significant impact on the separation and transfer of photogenerated carriers. In addition, Fig. 8c shows that the photocurrent onsets potential of the ZnO/CuO/Ag heterojunction gradually shifts to 0.025 V vs. RHE, compared with ZnO/CuO heterojunction (0.375 V vs. RHE). These shifts can be attributed to the Fermi level shift negatively [38] and the recombination

**Fig. 7** **a** Element distribution mapping of ZnO/CuO/Ag film and **b** EDS spectrum of the ZnO/CuO/Ag film. The inset is the atom percent of O, Cu, Ag, and Zn



**Fig. 8** UV–visible light absorption spectra of ZnO/CuO **a** and curves of  $(\alpha hv)^2$  vs.  $hv$  **b**; **c** current density–voltage ( $i$ – $v$ ) curves under simulated sunlight illumination and in dark; **d** electrochemical impedance spectroscopy



of electron–hole pairs decreases near the flat band potential [39] by CuO coating and SPR effect of Ag NPs. It is of great significance that the heterojunction has the more negative photocurrent onset potential, because it shows that the process of photoelectrochemical water splitting needs lesser applied potential. Figure 8d shows the photocurrent density of the samples rises or falls when the light is turned on/off instantaneously. Indicating that these samples are sensitive to visible light due to the carriers transmission of ZnO/CuO and ZnO/CuO/Ag are fast.

As shown in Fig. 9, the efficiency of Ag-modified ZnO/CuO photoanode is as high as 15%, which is 1.36 times than that of ZnO/CuO. In addition, higher efficiency is obtained at lower fixed potentials of ZnO/CuO/Ag than the original ZnO and ZnO/CuO heterojunctions. This is because that Ag NPs provide more photogenerated electrons for ZnO/CuO heterojunctions under illumination.

To confirm the carrier transport rate of three different materials, the surface photovoltage spectroscopy (SPV) measurement is performed. As shown in Fig. 10, it can be observed that the SPV response threshold of ZnO, ZnO/CuO, and ZnO/CuO/Ag are about 385 nm, 496 nm, and 500 nm, which is consistent with the UV–visible absorption spectrum in Figs. 5a and 8a. The peak of ZnO/CuO/Ag is highest, indicating that the carrier concentration is the largest, and the PEC performance of ZnO/CuO/Ag is greater than that of ZnO and ZnO/CuO.

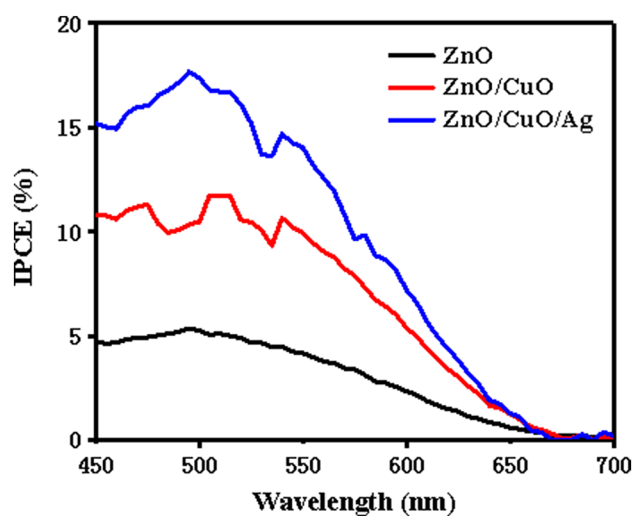


**Fig. 9** IPCE plot in the range of 450–700 nm measured at 1.23 V vs. RHE

To explain the excellent photoelectrochemical performance of ZnO/CuO/Ag heterojunction, the charges' transmission paths in ZnO/CuO/Ag heterojunction are investigated. The potential energy diagram for the ternary composite electrode is constructed, as shown in Fig. 11. In this ternary heterojunction, dendritic CuO is deposited on ZnO nanorods, and Ag NPs are uniformly attached to the surface of ZnO/CuO

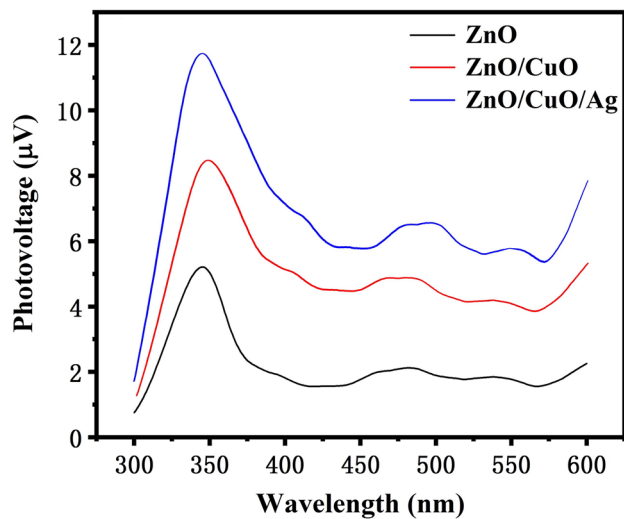


**Fig. 10** Surface photovoltage spectroscopy of ZnO, ZnO/CuO, and ZnO/CuO/Ag

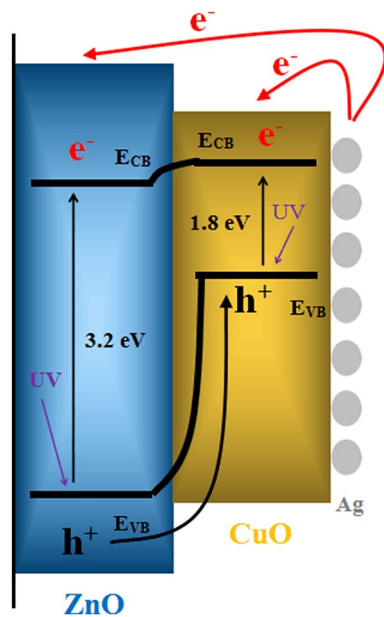


**Fig. 11** Schematic illustration of the bandgap energy diagram

heterojunction. In addition, the conduction band and valence band of CuO are more negative than the conduction band and valence band of ZnO, thus forming a gradient energy level in the ZnO/CuO heterojunction. The appropriate gradient energy levels can effectively suppress photogenerated carrier recombination. It is worth noting that Ag has SPR effect. On one hand, the SPR effect can enhance the absorption of light; on the other hand, it can capture electrons and inhibit the recombination of photogenerated electron–hole pairs. Since Ag has a higher work function than ZnO when Ag and ZnO are in contact, a Schottky barrier is formed between them. When the

Ag-doped ZnO/CuO film is illuminated, the photogenerated electrons generated in Ag will continue to transfer into ZnO and CuO under the action of Schottky barrier, thus effectively suppressing the recombination of electrons and holes. Finally, the photogenerated electrons are drawn to the external circuit. In addition, at the same time, the photogenerated holes formed in the valence band of ZnO are transferred through Ag particles into electrolyte.

Based on the above results, we propose the following possible reasons to explain the significant increase in the photoelectrochemical activity of ZnO/CuO/Ag photoelectrode: (i) the formation of a heterojunction can effectively expand visible light absorption range, and Ag NPs can also promote this process due to the surface plasmon resonance (SPR); (ii) the formation of a heterojunction can form a gradient energy level, which can better promote the separation of electron–hole pairs; and (iii) under visible light irradiation, Ag NPs can generate hot electrons due to the SPR effect, and the hot electrons are injected to the conduction bands of ZnO/CuO heterojunction which can make electron–hole pairs better separate.

## 4 Conclusion

In summary, in this paper, ZnO/CuO heterostructures have been successfully prepared by a chemical bath deposition method. Then, plasmonic Ag NPs were loaded onto the ZnO/CuO heterostructures. The ZnO/CuO/Ag heterojunction photoelectrode shows a higher photocurrent density ( $3.45 \text{ mA cm}^{-2}$  at 1.23 V vs. RHE), which is 3.08 and 1.12 times higher than that of ZnO and ZnO/CuO photoelectrode, respectively. In this system, the formation of a heterojunction can improve the absorption range and increase the electron–hole pairs' separation rate, and the loading of plasmonic Ag nanoparticles can expand the absorption range of visible light and generate more photogenerated electrons through surface plasmon resonance (SPR). The research results demonstrated a promising ternary semiconductor structure, which can expand the absorbance spectra range and increase the separation rate of photogenerated carriers to improve the photoelectric properties of photoanodes in photoelectrochemical (PEC) water-splitting system.

**Acknowledgements** The authors gratefully acknowledge financial support from Open Foundation of Hubei Collaborative Innovation Center for High-efficient Utilization of Solar Energy (No. HBSKFZD2017001).

## References

1. H. Xu, P. Reunchan, S.X. Ouyang, H. Tong, N. Umezawa, Anatase  $\text{TiO}_2$  single crystals exposed with high-reactive 111 facets toward efficient  $\text{H}_2$  evolution. *Chem. Mater.* **25**, 405–411 (2013)
2. Q.J. Xiang, J.G. Yu, Graphene-based photocatalysts for hydrogen generation. *J. Phys. Chem. Lett.* **4**, 753–759 (2013)



3. C.L. Yu, Q.Z. Fan, Y. Xie, J.C. Chen, Sonochemical fabrication of novel square-shaped F doped TiO<sub>2</sub> nanocrystals with enhanced performance in photocatalytic degradation of phenol. *J. Hazard. Mater.* **237**, 38–45 (2012)
4. K. Iwashina, A. Iwase, Y.H. Ng, Z-schematic water splitting into H<sub>2</sub> and O<sub>2</sub> using metal sulfide as a hydrogen-evolving Photocatalyst and reduced graphene oxide as a solid-state electron mediator. *J. Am. Chem. Soc.* **137**, 604–607 (2015)
5. B. Jiang, L.L. Jiang, X.W. Shi, W.C. Wang, G.S. Li, Ag<sub>2</sub>O/TiO<sub>2</sub> nanorods heterojunctions as a strong visible-light photocatalyst for phenol treatment. *J. Sol-Gel. Sci. Technol.* **73**, 314–321 (2015)
6. A. Fujishima, K. Honda, Electrochemical photolysis of water at a semiconductor electrode. *Nature* **238**, 37–38 (1972)
7. Y. Li, Z.F. Liu, Y. Wang, Z.C. Liu, J.H. Han, J. Ya, ZnO/CuInS<sub>2</sub> core/shell heterojunction nanorod for photoelectrochemical water splitting. *Int. J. Hydrogen Energy* **37**, 15029–15037 (2012)
8. D. Chen, Z.F. Liu, M. Zhou, P.D. Wu, J.D. Wei, Enhanced photoelectrochemical water splitting performance of  $\alpha$ -Fe<sub>2</sub>O<sub>3</sub> nanostructures modified with Sb<sub>2</sub>S<sub>3</sub> and cobalt phosphate. *J. Alloy. Compd.* **742**, 918–927 (2018)
9. J.D. Wei, C.L. Zhou, Y. Xin, X.F. Li, L. Zhao, Z.F. Liu, Cooperation effect of heterojunction and co-catalyst in BiVO<sub>4</sub>/Bi<sub>2</sub>S<sub>3</sub>/NiOOH photoanode for improving photoelectrochemical performances. *New J. Chem.* **42**, 19415–19422 (2018)
10. Y. Wang, R. Shi, J. Lin, Y.F. Zhu, Enhancement of photocurrent and photocatalytic activity of ZnO hybridized with graphite-like C<sub>3</sub>N<sub>4</sub>. *Energy Environ. Sci.* **4**, 2922–2929 (2011)
11. J.W. Zhou, M. Zhang, Y.F. Zhu, Preparation of visible light-driven g-C<sub>3</sub>N<sub>4</sub>@ZnO hybrid photocatalyst via mechanochemistry. *Phys. Chem. Chem. Phys.* **16**, 17627–17633 (2014)
12. D.M. Chen, K.W. Wang, D.G. Xiang, R.L. Zong, W.Q. Yao, Y.F. Zhu, Significantly enhancement of photocatalytic performances via core-shell structure of ZnO@mpg-C<sub>3</sub>N<sub>4</sub>. *Appl. Catal. B* **147**, 554–561 (2014)
13. M. Law, L.E. Greene, J.C. Johnson, R. Saykally, P.D. Yang, Nanowire dye-sensitized solar cells. *Nat. Mater.* **4**, 455–459 (2005)
14. J.R. Xiao, X.L. Zhang, Y.D. Li, A ternary g-C<sub>3</sub>N<sub>4</sub>/Pt/ZnO photoanode for efficient photoelectrochemical water splitting. *Int. J. Hydrogen Energy* **40**, 9080–9087 (2015)
15. Q.Z. Wang, T.J. Niu, L. Wang, FeF<sub>2</sub>/BiVO<sub>4</sub> heterojunction photoelectrodes and evaluation of its photoelectrochemical performance for water splitting. *Chem. Eng. J.* **337**, 506–514 (2018)
16. N. Son, J.Y. Do, M. Kang, Characterization of core@shell-structured ZnO@Sb<sub>2</sub>S<sub>3</sub> particles for effective hydrogen production from water photo spitting. *Ceram. Int.* **14**, 11250–11259 (2017)
17. A. Rokade, S. Rondiya, A. Date, V. Sharma, M. Prasad, H. Pathan, S. Jadkar, Electrochemical synthesis of core-shell ZnO/CdS nanostructure for photocatalytic water splitting application. *Energy Proc.* **110**, 121–127 (2017)
18. D. Chen, Z.F. Liu, Z.G. Guo, W.G. Yan, Y. Xin, Enhancing light harvesting and charge separation of Cu<sub>2</sub>O photocathodes with spatially separated noble-metal cocatalysts towards highly efficient water splitting. *J. Mater. Chem. A* **6**, 20393–20401 (2018)
19. K.H. Ng, H.A. Kadir, L.J. Minggu, M.B. Kassim, Stability of WO<sub>3</sub>/CuO heterojunction photoelectrodes in PEC system. *Mater. Sci. Forum* **756**, 219–224 (2013)
20. S.B. Wang, C.H. Hsiao, S.J. Chang, Z.Y. Jiao, S.J. Young, ZnO branched nanowires and the p-CuO/n-ZnO heterojunction nanostructured photodetector. *IEEE Trans. Nanotechnol.* **12**, 263–269 (2013)
21. W.B. Hou, W.H. Hung, P. Pavaskar, Synthesis of strong light scattering absorber of TiO<sub>2</sub>-CMK-3/Ag for photocatalytic water splitting under visible light irradiation. *ACS Catal.* **1**, 929–936 (2011)
22. F. Lin, D. Wang, Z. Jiang, Photocatalytic oxidation of thiophene on BiVO<sub>4</sub> with dual co-catalysts Pt and RuO<sub>2</sub> under visible light irradiation using molecular oxygen as oxidant. *Energy Environ. Sci.* **5**, 6400–6406 (2012)
23. B.J. Ma, J.H. Yang, H.X. Han, J.T. Wang, X.H. Zhang, C. Li, Enhancement of photocatalytic water oxidation activity on IrO<sub>x</sub>-ZnO/Zn<sub>2-x</sub>GeO<sub>4-x-3y</sub>N<sub>2y</sub> catalyst with the solid solution phase junction. *J. Phys. Chem. C* **114**, 12818–12822 (2010)
24. H. Yan, J. Yang, G. Ma, G.P. Wu, X. Zong, Z.B. Lei, J.Y. Shi, C. Li, Visible-light-driven hydrogen production with extremely high quantum efficiency on Pt-PdS/CdS photocatalyst. *J. Catal.* **266**, 165–168 (2009)
25. J.H. Yang, D. Wang, H.X. Han, A cocatalyst-free CdS nanorod/ZnS nanoparticle composite for high-performance visible-light-driven hydrogen production from water. *Acc. Chem. Res.* **46**, 2355–2364 (2013)
26. R. Su, R. Tiruvalam, Q. He, Promotion of phenol photodecomposition over TiO<sub>2</sub> using Au, Pd, and Au-Pd nanoparticles. *ACS Nano* **6**, 6284–6292 (2012)
27. D. Shiraishi, Y. Tsukamoto, A. Sugano, Platinum nanoparticles supported on anatase titanium dioxide as highly active catalysts for aerobic oxidation under visible light irradiation. *ACS Catalysis* **2**, 1984–1992 (2012)
28. H.Y. Chen, K.W. Liu, L.F. Hu, A.A. Al-Ghamdi, X.H. Fang, New concept ultraviolet photodetectors. *Mater. Today* **18**, 493–502 (2015)
29. A. Ahmadivand, N. Pala, D.Ö. Güney, Enhancement of photothermal heat generation by metallodielectric nanoplasmonic clusters. *Opt. Express* **23**, A682–A691 (2015)
30. M. Tanzid, A. Ahmadivand, R. Zhang, B. Cerjan, A. Sobhani, Combining plasmonic hot carrier generation with free carrier absorption for high-performance near-infrared silicon-based photodetection. *ACS Photon.* **5**, 3472–3477 (2018)
31. B.F. Zheng, T. Ouyang, Z. Wang, J.Y. Long, Y.B. Chen, Z.Q. Liu, Enhanced plasmon-driven photoelectrocatalytic methanol oxidation on Au decorated  $\alpha$ -Fe<sub>2</sub>O<sub>3</sub> nanotube arrays. *Chem. Commun.* **69**, 9583–9586 (2018)
32. Z. Kang, X.Q. Yan, Y.F. Wang, Y.G. Zhao, Z.M. Bai, Y.C. Liu, K. Zhao, S.Y. Cao, Y. Zhang, Self-powered photoelectrochemical biosensing platform based on Au NPs@ZnO nanorods array. *Nano Res.* **9**, 344–352 (2016)
33. D. Chaudhary, S. Singh, V.D. Vankar, N. Khare, A ternary Ag/TiO<sub>2</sub>/CNT photoanode for efficient photoelectrochemical water splitting under visible light irradiation. *Int. J. Hydrogen Energy* **12**, 7826–7835 (2017)
34. Z. Liu, Q. Cai, C. Ma, J. Zhang, J.Q. Liu, Photoelectrochemical properties and growth mechanism of varied ZnO nanostructures. *New J. Chem.* **41**, 7947–7952 (2017)
35. I. Grigioni, K.G. Stamplecoskie, E. Selli, Dynamics of photogenerated charge carriers in WO<sub>3</sub>/BiVO<sub>4</sub> heterojunction photoanodes. *J. Phys. Chem. C* **119**, 20792–20800 (2015)
36. S. Link, M.A. El-Sayed, Spectral properties and relaxation dynamics of surface plasmon electronic oscillations in gold and silver nanodots and nanorods. *J. Phys. Chem. B* **103**, 8410–8426 (1999)
37. L.Q. Jing, Z.H. Sun, F.L. Yuan, The effects of La and Cu doping on the photogenerated charges over nano-TiO<sub>2</sub> and the relationship between photocatalytic activity and photogenerated charges. *Sci. Chin. Chem.* **36**, 53–57 (2006)
38. J. Luo, L. Ma, T. He, S. Wang, H. Sun, H.J. Fan, TiO<sub>2</sub>/(CdS, CdSe, CdSeS) nanorod heterostructures and photoelectrochemical properties. *J. Phys. Chem. C* **116**, 11956–11963 (2012)
39. E.M.P. Steinmiller, K.S. Choi, Photochemical deposition of cobalt-based oxygen evolving catalyst on a semiconductor photoanode for solar oxygen production. *Proc. Natl. Acad. Sci.* **106**, 20633–20636 (2009)